

## Dynamic stabilization of perovskites at elevated temperatures: A comparison between cubic BaFeO<sub>3</sub> and vacancy-ordered monoclinic BaFeO<sub>2.67</sub>

Yongliang Ou ,\* Yuji Ikeda , Oliver Clemens , and Blazej Grabowski   
Institute for Materials Science, University of Stuttgart, 70569 Stuttgart, Germany

 (Received 27 May 2022; accepted 4 August 2022; published 31 August 2022)

The impact of ordered vacancies on the dynamic stability of perovskites is investigated under the *ab initio* framework with a focus on cubic BaFeO<sub>3</sub> ( $Pm\bar{3}m$ ) and vacancy-ordered monoclinic BaFeO<sub>2.67</sub> ( $P2_1/m$ ). The harmonic approximation shows that both structures are dynamically unstable at 0 K. For the monoclinic structure, the instability is related to rotational distortions of the Fe coordination tetrahedra near the ordered vacancies. *Ab initio* molecular dynamics simulations in combination with the introduced structural descriptor demonstrate that both structures are stabilized above 130 K. Our results suggest that the ordered vacancies do not significantly alter the critical temperature at which Ba-Fe-O perovskites are dynamically stabilized. Furthermore, strong anharmonicity for the vacancy-ordered structure above its critical temperature is revealed by a significant asymmetry of the trajectories of O anions near the ordered vacancies.

DOI: [10.1103/PhysRevB.106.064308](https://doi.org/10.1103/PhysRevB.106.064308)

### I. INTRODUCTION

Vacancy-ordered perovskites attract increasing attention in fields such as optoelectronics [1], photovoltaics [2], and electrochemistry [3,4] due to their tunable electronic, magnetic, and catalytic properties. The versatility of these materials is related to a stability competition among various structural arrangements. The Ba-Fe-O system offers a particularly rich class of perovskite-type structures with various vacancy orderings, e.g., hexagonal BaFeO<sub>2.65</sub> ( $P6_3/mmc$ ) [5], monoclinic BaFeO<sub>2.5</sub> ( $P2_1/c$ ) [6], or BaFeO<sub>2.67</sub> ( $P2_1/m$ ) [7].

Despite considerable experimental efforts, the actual vacancy ordering and, thus, the exact arrangement of the atoms in the nonstoichiometric Ba-Fe-O phases is often not resolved [6] on account of the structural complexity introduced by the vacancies. Experiments face practical challenges, e.g., in achieving high phase purity or in coping with multistage phase transitions that hinder the observation of single phases in extended temperature intervals [7]. From a more fundamental perspective, it is the intricate interplay of vacancy ordering and the dynamic stability that poses a decisive challenge.

Traditionally, the Goldschmidt tolerance factor [8] and its extended forms [9–11], most of which take the chemical formula and the ionic radii as the basic input data, have been used to predict the dynamic stability of perovskites. These empirical rules are, however, oversimplified and, hence, insufficient to reveal the details of the dynamic stability. For example, they are not applicable to vacancy-ordered structures and, likewise, they do not predict the dynamic stabilization at elevated temperatures. In order to properly take such features into account, *ab initio* simulations, specifically in the form of density-functional theory (DFT), are required.

In *ab initio* simulations, the harmonic approximation is commonly used to determine the dynamic (in)stability at 0 K [12]. Indeed, for BaFeO<sub>3</sub> (i.e., the “perfect” cubic perovskite without ordered vacancies), a few studies have been reported to date as summarized in Table I, specifically employing the DFT +  $U$  approach [13]. DFT +  $U$  is computationally much more affordable than DFT supplemented with advanced hybrid functionals, but an additional input parameter, i.e.,  $U_{\text{eff}}$ , is needed to correct the overdelocalization error of the standard exchange-correlation functionals of DFT.

A proper  $U_{\text{eff}}$  value is not trivial to determine. Typically, experimental bulk properties, such as the lattice parameters, the magnetic moments, and the bulk moduli are considered to decide on  $U_{\text{eff}}$  [15–18]. The, thus, obtained  $U_{\text{eff}}$  values are, however, not necessarily suitable for dynamic stability investigations. A general problem is, as Table I reveals, that a small change in  $U_{\text{eff}}$  can lead to qualitatively different stabilities. For example, cubic BaFeO<sub>3</sub> was predicted to be dynamically stable with  $U_{\text{eff}} \approx 5$  eV [15,17], whereas Jahn-Teller distortions were observed with  $U_{\text{eff}} = 4$  eV [16,18]. These differences highlight that the  $U_{\text{eff}}$  value needs to be chosen with care, ideally by calibration with respect to a higher level method. For vacancy-ordered Ba-Fe-O perovskites (i.e., compositions with lower O content than BaFeO<sub>3</sub>), *ab initio* investigations of the dynamic (in)stability have not been available until now.

Dynamic stabilization at finite temperatures can be investigated via *ab initio* molecular dynamics (AIMD) simulations. One type of approaches utilizes effective force constants extracted from AIMD. For example, the temperature-dependent effective potential method [23] fits effective harmonic force constants to the forces generated by AIMD. With the self-consistent phonon method, Tadano and Tsuneyuki [24] showed how to obtain renormalized phonon frequencies from anharmonic force constants extracted from AIMD. In general, sufficiently long AIMD runs are required for these methods to obtain reliable results especially for

\*yongliang.ou@imw.uni-stuttgart.de

TABLE I. Theoretical studies of the dynamic stability of Ba-Fe-O perovskites at 0 K. Cubic (cub.) BaFeO<sub>3</sub> is ferromagnetic (FM) whereas monoclinic (mon.) BaFeO<sub>2.67</sub> is G-type (in the Wollan-Koehler notation [14]) antiferromagnetic (AFM).

Year	Phase	Method	$U_{\text{eff}}$ (eV)	Stability
2017 [15]	Cub. BaFeO <sub>3</sub>	PBE <sup>a</sup> + $U$	5	Stable
2018 [16]	Cub. BaFeO <sub>3</sub>	PBE + $U$	4	Unstable
2018 [17]	Cub. BaFeO <sub>3</sub>	PBEsol <sup>b</sup> + $U$	5.2	Stable
2021 [18]	Cub. BaFeO <sub>3</sub>	PBE + $U$	4	Unstable
This paper	Cub. BaFeO <sub>3</sub>	HSE06 <sup>c</sup>	N/A	Unstable
This paper	Cub. BaFeO <sub>3</sub>	PBE + $U$	3	Unstable
This paper	Mon. BaFeO <sub>2.67</sub>	PBE + $U$	3	Unstable

<sup>a</sup>Perdew-Burke-Ernzerhof (PBE) exchange-correlation functional [19].

<sup>b</sup>Revised PBE exchange-correlation functional for solids [20,21].

<sup>c</sup>Heyd-Scuseria-Ernzerhof (HSE) hybrid functional [22].

materials with significant anharmonicity. Another strategy is to analyze the lattice distortions of the structures directly with AIMD. The dynamic stabilization can be then visualized explicitly as a function of temperature, and the anharmonic contribution can be fully considered. Such an approach was applied to cubic perovskites [25,26], although not yet to vacancy-ordered perovskites.

The aim of the present paper is to compare the dynamic stability of cubic BaFeO<sub>3</sub> ( $Pm\bar{3}m$ ) [27] (no ordered vacancies) with vacancy-ordered monoclinic BaFeO<sub>2.67</sub> ( $P2_1/m$ ) [7] at 0 K and at finite temperatures with AIMD and, thereby, to reveal the impact of ordered vacancies on the dynamic stability of perovskites. We first demonstrate that  $U_{\text{eff}} = 3$  eV should be chosen since it well reproduces the dynamic instability predicted by the more accurate HSE06 hybrid functional [28,29]. Based on the optimized  $U_{\text{eff}}$ , we investigate the link between the ordered vacancies and the imaginary harmonic phonon modes at 0 K. We analyze trajectories of the atoms near the ordered vacancies at finite temperatures and investigate the influence of the ordered vacancies on the stabilization mechanism. To this end, we introduce a structural descriptor that captures the temperature-driven transformation for both the vacancy-free cubic and vacancy-ordered monoclinic structures.

## II. METHODOLOGY

### A. Cubic and monoclinic structures

Figure 1(a) shows the utilized simulation cell of the ideal cubic BaFeO<sub>3</sub> structure. Whereas the unit cell contains five atoms, in the present work, a  $2 \times 2 \times 2$  supercell (40 atoms), which contains eight symmetrically equivalent corner-shared regular Fe coordination octahedra, was considered to capture the structural distortion at a low temperature. Each octahedron consists of one central Fe atom and six surrounding O atoms. Ba atoms are located between the octahedra.

To derive the vacancy-ordered structure, a coordinate transformation [4,7,30] is performed on the unit cell of the cubic structure. The lattice vectors of the transformed unit cell  $\mathbf{a}_{\text{cub}'}$ ,  $\mathbf{b}_{\text{cub}'}$ , and  $\mathbf{c}_{\text{cub}'}$  are related to that of the original unit cell  $\mathbf{a}_{\text{cub}}$ ,

$\mathbf{b}_{\text{cub}}$ , and  $\mathbf{c}_{\text{cub}}$  as

$$\begin{pmatrix} \mathbf{a}_{\text{cub}'} \\ \mathbf{b}_{\text{cub}'} \\ \mathbf{c}_{\text{cub}'} \end{pmatrix} = \begin{pmatrix} -1 & -1 & 2 \\ 1 & -1 & 0 \\ 1 & 1 & 1 \end{pmatrix} \begin{pmatrix} \mathbf{a}_{\text{cub}} \\ \mathbf{b}_{\text{cub}} \\ \mathbf{c}_{\text{cub}} \end{pmatrix}. \quad (1)$$

While this transformation leads to a six-times larger unit cell, to simulate the dynamic stability of the vacancy-ordered structure as well as to realize the G-type AFM ordering (see Sec. II C for details), it was further expanded by  $1 \times 1 \times 2$ . The, thus, obtained simulation cell contains 12 corner-shared regular Fe coordination polyhedra as shown in Fig. 1(b). The orientation relationship between the two unit cells is shown in Fig. 1(c).

The (010)<sub>cub'</sub> plane projection of the transformed cubic structure with four highlighted octahedra is shown in Fig. 1(d). Ordered vacancies are created by removing the four O atoms belonging to these four octahedra as shown in Fig. 1(e). The composition of the supercell changes from Ba<sub>12</sub>Fe<sub>12</sub>O<sub>36</sub> to Ba<sub>12</sub>Fe<sub>12</sub>O<sub>32</sub>, i.e., the formula unit (f.u.) changes from BaFeO<sub>3</sub> to BaFeO<sub>2.67</sub>. After the formation of the vacancies, four of the 12 previously octahedrally coordinated Fe cations become tetrahedrally coordinated. The symmetry of the structure is lowered, and the space group is changed to monoclinic  $P2_1/m$ . As a final step, the vacancy-ordered structure is optimized in an *ab initio* manner, during which relaxation of the four tetrahedra and a shear of the supercell in the [100]<sub>mon</sub> direction take place as shown in Fig. 1(f).

### B. Structural descriptor $\Delta$

To quantify the displacive phase transformation at the atomistic level, we introduce a structural descriptor  $\Delta$  along similar lines as performed previously for materials showing the bcc- $\omega$  phase transformation [32–34]. The key requirements are as follows:

(1) The structural descriptor  $\Delta(T)$  is a temperature-dependent scalar value that condenses the relevant information on the displacive phase transformation from AIMD trajectories.

(2) Thermal vibrations (i.e., random displacements) are filtered out to a good degree to increase the contrast in  $\Delta$  between the low-symmetry phase at a low temperature and the high-symmetry phase at a high temperature.

(3) Atomic displacements irrelevant to symmetry breaking are filtered out in order to distinguish the structure from the structures belonging to different space groups.

(4) The vacancy-free cubic and the vacancy-ordered monoclinic structure are treated on an equal footing, i.e., O anions in octahedral environments are considered similarly to those in tetrahedral environments.

To fulfill these requirements we define  $\Delta$  as follows. For a polyhedron composed of a central Fe cation  $i$  and surrounding O anions labeled with  $j$ , the temperature-dependent relative position vectors  $\mathbf{r}_{ij}(T)$  are defined as

$$\mathbf{r}_{ij}(T) = \langle \mathbf{R}_j \rangle_T - \langle \mathbf{R}_i \rangle_T, \quad (2)$$

where  $\mathbf{R}_i$  is the position vector of the  $i$ th cation and  $\mathbf{R}_j$  of the  $j$ th anion. The time-averaged position of an ion at a given temperature  $T$  is represented by  $\langle \cdots \rangle_T$ . Figures 2(a) and 2(b) give examples of the relative position vectors  $\mathbf{r}_{ij}$  for the octahedral and the tetrahedral coordinations, respectively. Based on the

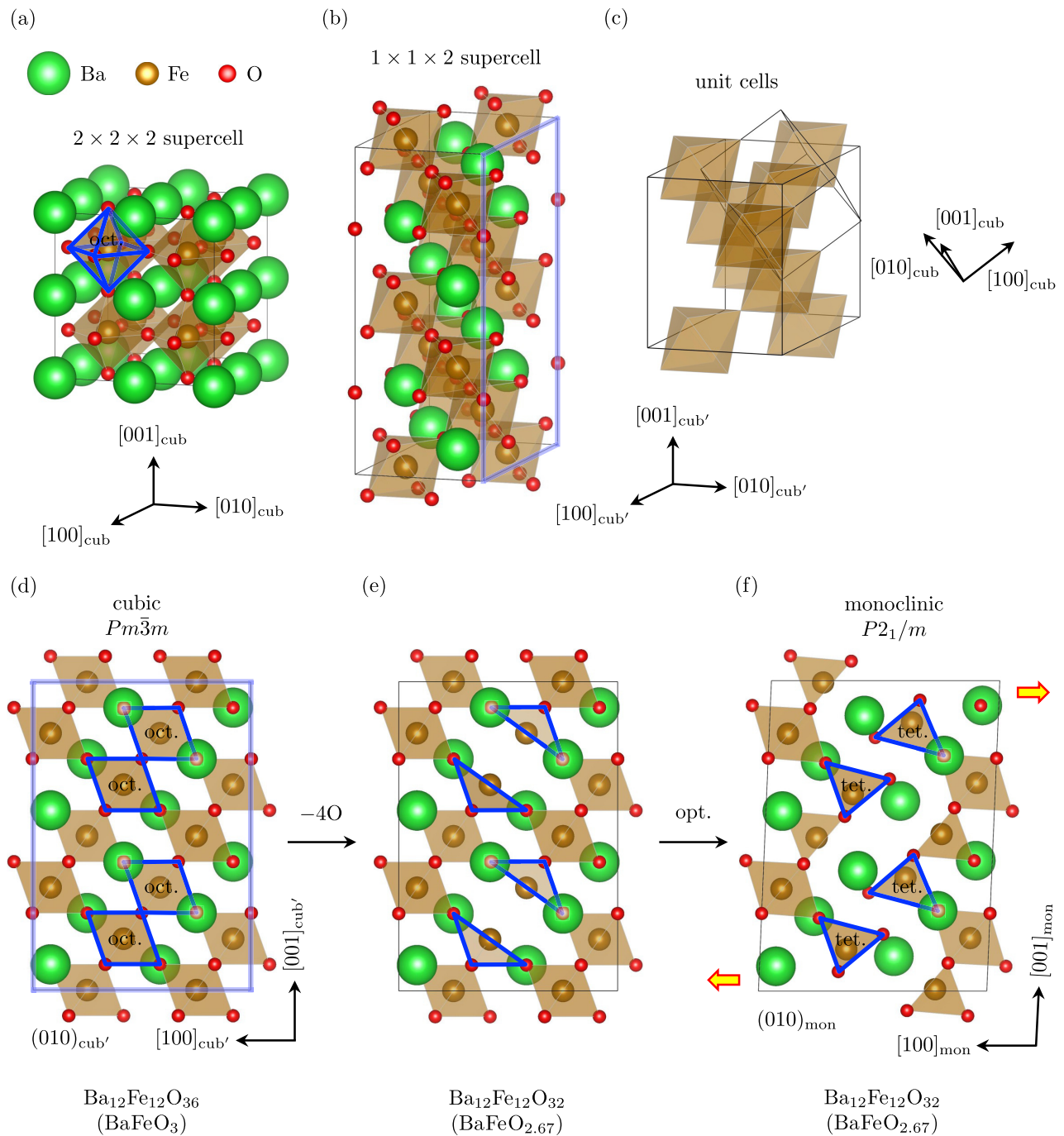


FIG. 1. Derivation of the vacancy-ordered monoclinic structure from the cubic structure. (a) Simulation cell ( $2 \times 2 \times 2$  supercell) of the cubic structure. (b) Simulation cell ( $1 \times 1 \times 2$  supercell) after coordinate transformation. (c) Orientation comparison of the original and the transformed unit cells. (d)  $(010)_{cub'}$  plane projection of the supercell (b) with the four highlighted octahedra. (e) Vacancy creation on the O sites. (f) Simulation cell ( $1 \times 1 \times 2$  supercell) of the monoclinic structure with indication of the shearing during the structural optimization process. The numbers of atoms (f.u.) in the cells are shown below for (d)–(f). Crystal structures are visualized by VESTA [31].

relative position vectors  $\mathbf{r}_{ij}$ , we define a structure-dependent projection as

$$p_{ij} = \begin{cases} \mathbf{r}_{ij} \cdot \hat{\mathbf{r}}_{ij}, & \text{cubic,} \\ \mathbf{r}_{ij} \cdot \hat{\mathbf{u}}_{[010]_{\text{mon}}}, & \text{monoclinic,} \end{cases} \quad (3)$$

$$p_{ij} = \begin{cases} \mathbf{r}_{ij} \cdot \hat{\mathbf{r}}_{ij}, & \text{cubic,} \\ \mathbf{r}_{ij} \cdot \hat{\mathbf{u}}_{[010]_{\text{mon}}}, & \text{monoclinic,} \end{cases} \quad (4)$$

which gives the parameter  $p_{ij}$ . The relative position vector  $\mathbf{r}_{ij}$  is projected onto the unit vectors in the same direction of  $\mathbf{r}_{ij}$  ( $\hat{\mathbf{r}}_{ij}$ ) for the cubic structure and in the symmetry bro-

ken direction ( $\hat{\mathbf{u}}_{[010]_{\text{mon}}}$ ) for the monoclinic structure. The structure-specific projection resulting in the two Eqs. (3) and (4) is necessary to fulfill in particular the third of the above-stated requirements on the structural descriptor.

To emphasize the distortion, the parameter of the ideal structure  $p^{\text{ideal}}$  is subtracted from the obtained temperature-dependent parameters  $p_{ij}$ . The structural descriptor is obtained as the mean value of the referenced  $p_{ij}$  parameters

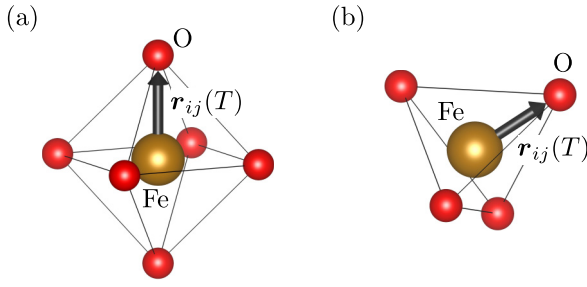


FIG. 2. Illustration of relative position vectors in (a) the octahedral and (b) the tetrahedral Fe-O coordination polyhedra.

of the cation-anion pairs inside the polyhedra,

$$\Delta = \frac{1}{IJ} \sum_{i=1}^I \sum_{j=1}^J |p_{ij} - p^{\text{ideal}}|, \quad (5)$$

where  $I$  is the number of cations and  $J$  is the number of anions surrounding each cation.

The ideal cubic structure belongs to the space-group  $Pm\bar{3}m$  (No. 221), and all O atoms are at the Wyckoff site  $3c$  for which all three fractional coordinates are fixed. This means that the space group of the cubic structure restricts each O atom to a single spatial point in the simulation cell. The elongation or contraction of a cation-anion bonding in all directions belongs to the distortion of the cubic structure. Therefore, the relative position vector  $r_{ij}(T)$  is projected to itself, i.e., the module of  $r_{ij}$  is calculated [Eq. (3)]. All Fe-O bondings in each of the octahedra in the simulation cell are taken into account for Eq. (5).

For the monoclinic structure, not all atoms are spatially restricted by the symmetry operations included in the space group, i.e., the structure can still belong to the same space group  $P2_1/m$  as long as the displacements of atoms do not break the symmetry. As will be discussed in Sec. III B, the dynamic instability of the monoclinic structure is mainly related to the distortion of the four tetrahedra in which only the four O atoms moving in the  $[010]_{\text{mon}}$  direction contribute to the symmetry breaking. To investigate the dynamic instability of  $P2_1/m$  BaFeO<sub>2.67</sub>, we, therefore, consider the Fe-O pairs [Fig. 2(b)] involving the four O atoms to compute  $\Delta$  and to, thus, evaluate the structural distortion. Mathematically, the four  $r_{ij}(T)$ 's [Eq. (2)] are projected to the unit vector along the  $[010]_{\text{mon}}$  direction [Eq. (4)], and  $I = 4$ ,  $J = 1$  in Eq. (5).

### C. Computational details

Spin alignment is important for Fe oxides. Experiments revealed that cubic BaFeO<sub>3</sub> has an A-type spiral spin structure near 0 K [27], which was, subsequently, investigated by *ab initio* simulations [35]. Furthermore, a magnetic transition to the FM state was observed experimentally at 111 K [27]. The FM state was also shown to be energetically the most stable within calculations with collinear spin alignment [36–38]. For the vacancy-ordered monoclinic BaFeO<sub>2.67</sub> structure, experimental and *ab initio* results show agreement on a G-AFM ordering [7]. In the present paper, collinear spin alignment was applied, and the FM and the G-AFM states were considered for the cubic and the monoclinic phases, respectively.

Electronic structure calculations were carried out under the DFT framework using the projector augmented-wave method [39] as implemented in VASP [40–42]. Electrons in the atomic orbitals  $5s^25p^66s^2$  (Ba),  $3d^64s^2$  (Fe), and  $2s^22p^4$  (O) were treated as valance electrons. The HSE06 hybrid functional [22] was employed to predict high-accuracy data on the dynamic stability of the cubic BaFeO<sub>3</sub> perovskite. For perovskites, it is known that hybrid functionals give good agreement with experiment for various material properties, such as the band gap [28] and the phonon frequencies [29]. The HSE06 results were utilized to calibrate complementary DFT+ $U$  simulations [13] with the effective Hubbard potential ( $U_{\text{eff}}$ ) added to the  $d$  orbitals of the Fe ions on top of the generalized gradient approximation (GGA) in the PBE parametrization [19]. As detailed in Sec. III A,  $U_{\text{eff}} = 3$  eV reproduces well the phonon dispersion and the double-well potential of cubic BaFeO<sub>3</sub> obtained from HSE06, and, thus, this  $U_{\text{eff}}$  value was used throughout the subsequent DFT+ $U$  calculations. The first-order Methfessel-Paxton scheme [43] with a smearing width of 0.1 eV was used for structural optimization and force calculations, and the tetrahedron method with Blöchl corrections [44] was used for accurate energy calculations. The plane-wave cutoff was set to 520 eV. The reciprocal space was sampled by  $\Gamma$ -centered  $4 \times 4 \times 4$  and  $3 \times 6 \times 3$   $k$ -point meshes for the 40-atom cubic BaFeO<sub>3</sub> and the 54-atom monoclinic BaFeO<sub>2.67</sub> simulation cells, respectively. For the Kohn-Sham self-consistent calculation, the energy was minimized until the energy difference converged to less than  $10^{-5}$  eV per simulation cell. Ionic relaxation was performed with the conjugate gradient algorithm until the maximum residual force was less than  $10^{-2}$  eV  $\text{\AA}^{-1}$ .

The harmonic phonon dispersions at 0 K were calculated using the finite displacement method implemented in PHONOPY [12]. The displacement amplitude was set to  $10^{-2}$   $\text{\AA}$ . Tests show that better energy convergences do not significantly alter the results, so the current criterion ( $10^{-5}$  eV per simulation cell) was also used for the phonon calculations. The residual forces in the optimized structure were subtracted from the forces of the displaced structure for accurate calculations of the interatomic force constants.

AIMD simulations were conducted using the Langevin thermostat and the canonical ensemble implemented in VASP [40–42]. A time step of 2 fs, a friction coefficient of  $10 \text{ ps}^{-1}$ , and the Fermi-Dirac smearing adjusted to the MD temperature were utilized. For each AIMD step, the criterion for energy convergence was set to  $10^{-3}$  eV per simulation cell, and the atomic positions were calibrated to fix the center of mass. Other parameters were the same as those chosen for the electronic structure calculations. In total 5000 AIMD steps (10 ps) were performed, and the first 300 steps were discarded in the thermal averages and in the analyzed MD trajectories. Tests show that this number of steps is sufficient to achieve thermal equilibrium.

## III. RESULTS

### A. Cubic BaFeO<sub>3</sub>

Figure 3(a) shows the phonon dispersion at 0 K calculated using HSE06 for the cubic BaFeO<sub>3</sub> structure. As indicated

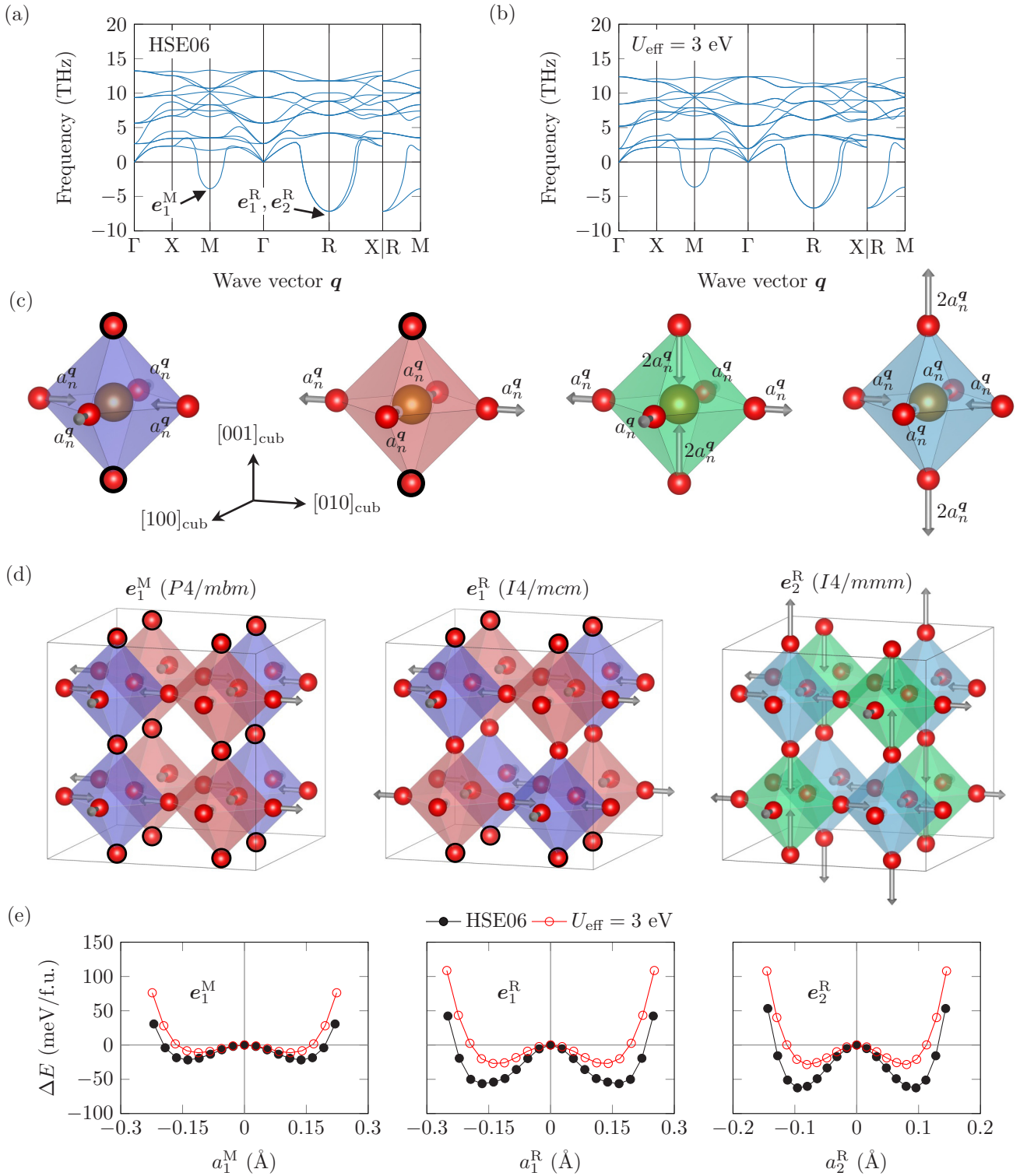


FIG. 3. Dynamic instability of the cubic structure at 0 K. Phonon dispersions calculated by (a) HSE06 and (b) DFT +  $U$  ( $U_{\text{eff}} = 3$  eV). Commensurate  $q$  points are indicated by tick labels. Negative frequencies indicate imaginary modes. (c) Four distortion types of an octahedron. Arrows indicate the movement of atoms. Stationary atoms are anchored by black circles. The superscript  $q$  and the subscript  $n$  are the wave vector and the band index, respectively. (d) Collective motion of atoms for the three imaginary modes indicated in (a). (e) Double-well potentials of the three imaginary modes. The corresponding displacements of the O atoms are indicated in (c).

by the arrows, one imaginary mode  $e_1^M$  at the M point [ $\mathbf{q} = (1/2, 1/2, 0)$ ] and two degenerate imaginary modes  $e_1^R$  and  $e_2^R$  at the R point [ $\mathbf{q} = (1/2, 1/2, 1/2)$ ] are observed, which reveals dynamic instability for the cubic structure at 0 K. The imaginary modes correspond to collective displacements on the O-atom sublattice. These displacements are related to the Jahn-Teller effect [16,18] and deform the octahedra in specific ways as illustrated in Figs. 3(c) and 3(d). There are, for example, breathing-type displacements in which the O atoms on one plane move simultaneously inward or outward. The displacements lower the symmetry, i.e., the space group changes from cubic  $Pm\bar{3}m$  to tetragonal  $P4/mbm$ ,  $I4/mcm$ , and  $I4/mmm$  for distortions along the  $e_1^M$ ,  $e_1^R$ , and  $e_2^R$  imaginary modes, respectively.

The double-well potentials corresponding to the imaginary modes are shown in Fig. 3(e) (black for HSE06). They reveal that the minimum in energy is reached already at a sub-angstrom level for any of the three imaginary modes. It can be also observed that the potential wells are rather shallow (few tenths of meV/f.u. which translates to a few meV/atom) such that the O anions should be able to overcome the potential barrier by thermal energy already at a low temperature. As shown later, AIMD simulations do confirm this statement.

Due to the high computational cost, it is practically difficult to utilize the accurate HSE06 hybrid functional for the AIMD simulations and for the vacancy-ordered monoclinic structure. This fact motivates the application of the computationally cheaper DFT +  $U$  approach. In the DFT +  $U$  method, dynamic stability of the Ba-Fe-O perovskites depends on the input parameter  $U_{\text{eff}}$  as discussed in Sec. I. In the present paper, the  $U_{\text{eff}}$  parameter has been calibrated by the just discussed HSE06 results. A range of  $U_{\text{eff}}$  values was tested with a focus on the phonon dispersion of the FM cubic structure (results are shown in Appendix A). The best match between the two methods is obtained with  $U_{\text{eff}} = 3$  eV, which is close to the value used by Wollstadt *et al.* [7]. A comparison between Figs. 3(a) and 3(b) exemplifies the good agreement for the phonon dispersion. The qualitative dependence of the imaginary branches is similar with quantitative differences of about 1 THz. The reasonable agreement between the potential energies [Fig. 3(e) red vs black] further supports the usage of  $U_{\text{eff}} = 3$  eV. DFT +  $U$  predicts a similar width and about half of the depth of the potential wells as compared with HSE06. Since the absolute energy difference at the lowest point of the potential well is quite small (less than 50 meV/f.u.), the DFT +  $U$  method with  $U_{\text{eff}} = 3$  eV is considered acceptable for the dynamic stability analysis.

To investigate the dynamic stability at elevated temperatures, AIMD simulations have been performed from 2 K up to 1500 K for the FM cubic BaFeO<sub>3</sub>. At low temperatures, large displacements are observed for the O anions as compared to the Ba or Fe cations, which reinforces the dynamic instability. The instability falls into the imaginary-mode regime identified from the phonon calculations, in which only O atoms show displacements [Figs. 3(c) and 3(d)]. Further relaxation (with fixed cell shape and volume) of the low-temperature distorted structure shows a decrease of the energy by  $-28.5$  meV/f.u. as compared to the ideal cubic structure, which is similar to the energy minimum of the potential wells of the  $e_2^R$  mode [ $-28.1$  meV/f.u., red lines in Fig. 3(e), cf.  $-26.9$  meV/f.u.

for  $e_1^R$  and  $-11.2$  meV/f.u. for  $e_1^M$ ]. Since all O atoms within the cubic structure are symmetrically equivalent, one specific O atom is used for demonstration as depicted in Fig. 4(a). The trajectories of the O anion at various temperatures are displayed in Fig. 4(b). At 2 K, the O anion is trapped at a displaced position in the  $x$  direction with a distance of about 0.1 Å. The potential barrier is overcome at about 30 K, and a relatively homogeneous distribution of the O anion is observed at 130 K and at higher temperatures.

To quantitatively describe the transformation observed in AIMD, we utilize the structure descriptor  $\Delta$  introduced in Sec. II B. Figure 4(c) shows the change in  $\Delta$  as a function of temperature. A sharp decrease in  $\Delta$  is observed just below 130 K, whereas it remains almost constant at higher temperatures. The AIMD simulations, thus, predict that the FM cubic structure is stabilized at about 130 K due to vibrational entropy. The local magnetic moment of Fe for the ideal cubic structure at 0 K is  $3.7 \mu_B$  per Fe ion. For all simulated temperatures, the FM spin state remains unchanged.

## B. Monoclinic BaFeO<sub>2.67</sub>

We now focus on the dynamic (in)stability of the more complex vacancy-ordered G-AFM monoclinic BaFeO<sub>2.67</sub> structure with the symmetry of  $P2_1/m$  [Fig. 1(f)]. Utilizing the accurate HSE06 functional for the respective stability analysis is challenging due to high computational requirements. As stated above, we, therefore, utilize the DFT +  $U$  method, and for consistency with the cubic BaFeO<sub>3</sub> simulations we choose  $U_{\text{eff}} = 3$  eV. (The impact of  $U_{\text{eff}}$  on the phonon dispersion of the monoclinic structure is discussed in Appendix B.)

The phonon dispersion of the monoclinic structure at 0 K is shown in Fig. 5(a). Since the simulation cell of the monoclinic structure is a  $1 \times 1 \times 2$  supercell, only two  $\mathbf{q}$  points in the reciprocal space, i.e.,  $\Gamma = (0, 0, 0)$  and  $Z = (0, 0, 1/2)$ , are commensurate points. Three and four imaginary modes are found for the  $\Gamma$  and  $Z$  points, respectively, which clearly reveals dynamic instability of the  $P2_1/m$  monoclinic structure at 0 K. Note that the relaxation applied during the construction process [Figs. 1(e) and 1(f)] cannot “remove” the dynamic instability observed in Fig. 5(a) due to symmetry constraints. The monoclinic structure after the relaxation corresponds to a saddle point on the potential energy surface (PES), and a vibrational mode analysis as performed here is necessary to detect the dynamic instability.

The analysis of the phonon eigenvectors shows that the first four imaginary modes [within  $-10$  to  $-5$  THz, indicated by arrows in Fig. 5(a)] mainly correspond to displacements of several specific O anions. The heavier Ba and Fe cations are involved in the other three imaginary modes (within  $-5$  to  $0$  THz). Since the lighter O atoms move faster than the Ba and Fe atoms, it seems reasonable to assume that the monoclinic structure is destabilized along a combination of the first four imaginary modes involving O atoms as the temperature is lowered. This assumption is indeed confirmed by the AIMD simulations (discussed in more detail below), which reveal that over 90% of the low-temperature distortion is contributed by these four lowest imaginary modes. With this we can also deduce that, after deforming along the four imaginary modes involving O atoms, the structure

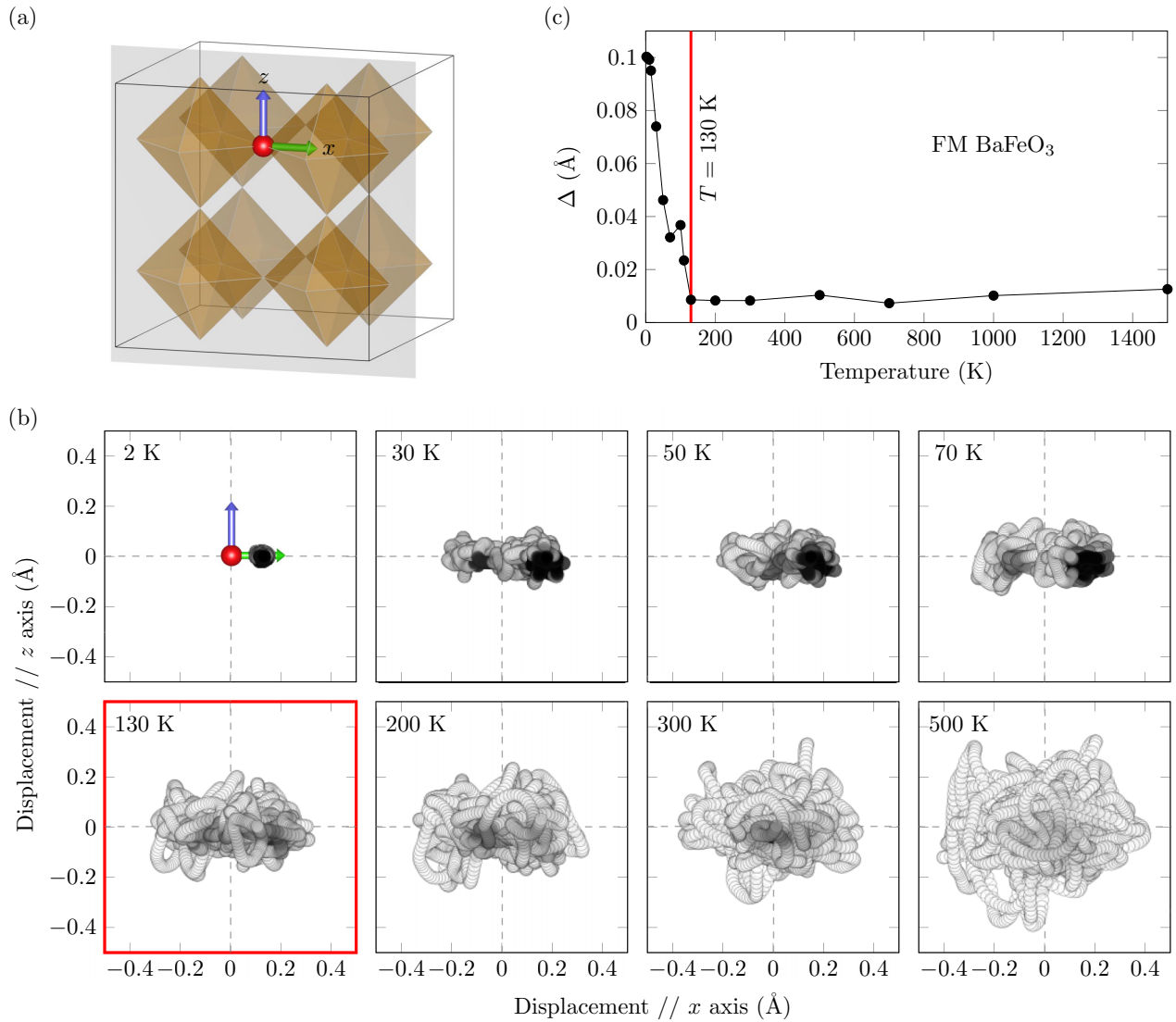


FIG. 4. AIMD simulation of the FM cubic BaFeO<sub>3</sub>. (a) Indication of one specific O atom. (b) Trajectories of the O anion at elevated temperatures. (c) The change in the structural descriptor as a function of temperature. The DFT +  $U$  method with  $U_{\text{eff}} = 3$  eV was used.

becomes dynamically stable along the other three imaginary modes involving Ba and Fe atoms through phonon-phonon interactions.

The four O-involving imaginary modes are visualized in real space in Figs. 5(c)–5(e) in which only the relevant parts of the monoclinic structure are displayed, specifically the four tetrahedra with their corresponding O atoms. These are the essential components describing the low-temperature distortion. The four imaginary modes can be built up from two types of symmetrically related deformations of the tetrahedra [Fig. 5(c)]. We recall that the tetrahedra arise due to the ordered vacancies and the subsequent relaxation [Figs. 1(d)–1(f)]. The instability of the monoclinic structure is, thus, related to the ordered vacancies.

The ideal monoclinic BaFeO<sub>2.67</sub> structure belongs to the space-group  $P2_1/m$  (No. 11). During the deformation of a tetrahedron, the O atom at the Wyckoff site  $2e$  is displaced by  $a_n^q$  along the  $[010]_{\text{mon}}$  direction, which breaks the reflection symmetry with respect to the  $(010)_{\text{mon}}$  plane and, thus, lowers

the symmetry from  $P2_1/m$  to, e.g.,  $P2_1$ . The two O atoms of the tetrahedron located at the Wyckoff site  $4f$  move along the  $[100]_{\text{mon}}$  direction, each by the same distance  $b_n^q$  but in opposite directions to each other. Their positions are not restricted by the space group. No quantitative relationship between  $a_n^q$  and  $b_n^q$  can be derived based on the analysis of the imaginary phonon modes.

Figure 5(b) shows the potential energy along the four O-involving imaginary modes. The double-well potentials affirm the dynamic instability of the ideal monoclinic structure at 0 K. These potential wells are shallower than those of the cubic structure [Fig. 3(e)], which, however, does not immediately mean that the monoclinic structure is easier to be stabilized at elevated temperatures. The true local minimum of the distorted monoclinic structure is not captured by displacements along single modes. Further relaxation of the low-temperature distorted structure (obtained from AIMD) gives a lower energy minimum of  $-16.1$  meV/f.u. at larger O-atom displacements (about  $0.2$  Å). Additionally, the

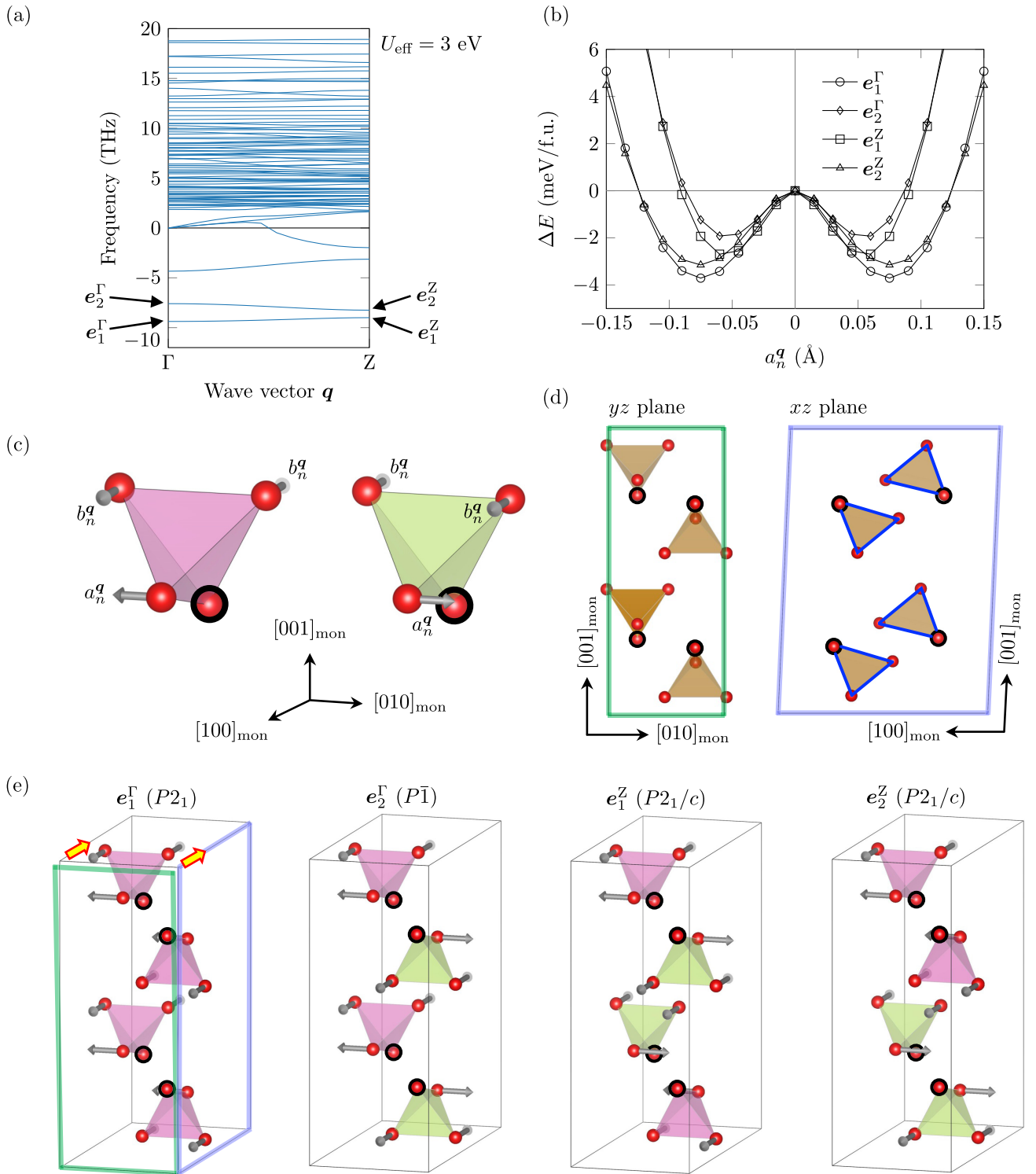


FIG. 5. Dynamic instability of the monoclinic structure at 0 K. (a) Phonon dispersion calculated by DFT +  $U$  ( $U_{\text{eff}} = 3 \text{ eV}$ ). The two points, i.e.,  $\Gamma = (0, 0, 0)$  and  $Z = (0, 0, 1/2)$ , are the commensurate  $q$  points with the present  $1 \times 1 \times 2$  supercell model. Negative frequencies indicate imaginary modes. (b) Double-well potentials of the four modes indicated in (a). The corresponding displacements of the O atoms are indicated in (c), where  $q$  and  $n$  are the wave vector and the band index, respectively. (c) Two distortion types of a tetrahedron. Arrows indicate the movement of atoms. Stationary atoms are anchored by black circles. (d) Projections of the optimized monoclinic structure [Fig. 1(f)] onto the  $yz$  and  $xz$  planes. Only the four highlighted tetrahedra and the O atoms forming them are displayed. (e) Collective motion of atoms for the four imaginary modes indicated in (a). Shearing of the simulation cell during the structural optimization process [Fig. 1(f)] is indicated.

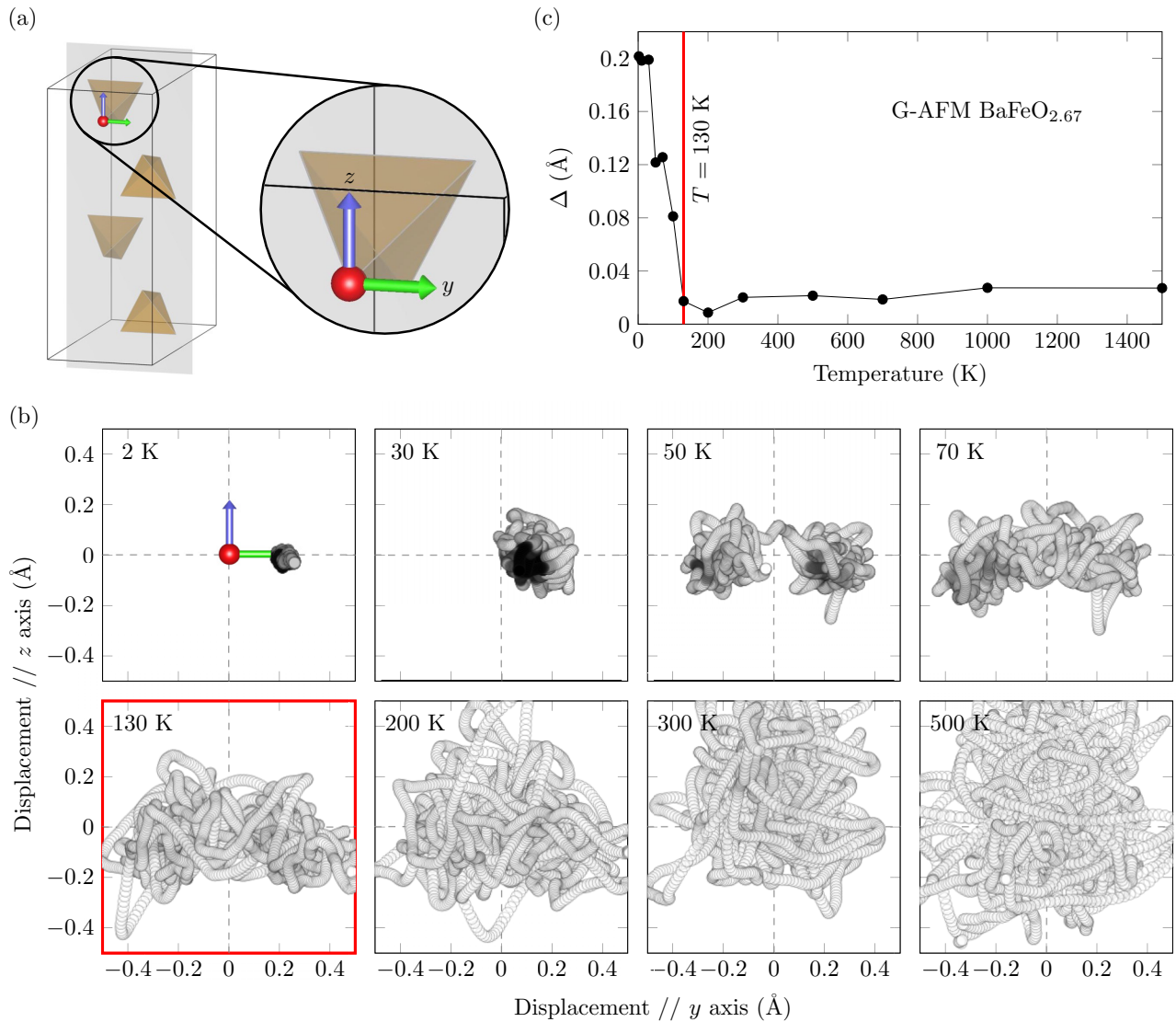


FIG. 6. AIMD simulation of the G-AFM vacancy-ordered monoclinic BaFeO<sub>2.67</sub>. (a) Indication of one specific O atom. (b) Trajectories of the O anion at elevated temperatures. (c) Structural descriptor  $\Delta$  as a function of temperature. The DFT +  $U$  method with  $U_{\text{eff}} = 3$  eV was used.

energy scales of the cubic and the monoclinic structures are not directly comparable because of the different formula units.

To properly capture the low-temperature displacive transformation and the corresponding dynamic stabilization at elevated temperatures, AIMD simulations have been performed from 2 K up to 1500 K for G-AFM BaFeO<sub>2.67</sub>. One of the O atoms involved in the low-temperature transformation is focused on for demonstration [Fig. 6(a)]. Figure 6(b) shows the trajectories of this O atom at various temperatures. At 2 K, the O atom is trapped in a displaced position in the  $y$  direction at a distance of about 0.2 Å, which once more substantiates the dynamic instability of the G-AFM monoclinic structure at low temperatures. At 50 K the O atom is able to pass the barrier to the other side within the available simulation time. As the temperature further increases, the O atom can frequently cross the barrier until the trajectory becomes homogeneously spread over a larger region (about 130 K) with no more obvious

signs of the displacement (i.e., the average position of the O anion gradually shifts to the ideal position). It is noteworthy that for temperatures 130 K and higher the trajectories become asymmetric along the  $z$  axis (which is perpendicular to the double-well potential along  $y$ ) with an increased probability to find the O anion at positive  $z$  displacements. This finding indicates that the PES is asymmetric along the  $z$  direction.

To quantify the transformation, we utilize again the structure descriptor  $\Delta$  extracted from the AIMD simulations. Figure 6(c) reveals a similar temperature dependence of  $\Delta$  as observed for the cubic structure. In particular, the original  $P2_1/m$  monoclinic structure is stabilized at 130 K due to vibrational entropy. For the ideal monoclinic structure at 0 K, the local magnetic moment for the tetrahedrally coordinated Fe ion is  $3.6 \mu_B$ , and for the other two types of Fe ions the moments are  $3.9 \mu_B$  and  $4.0 \mu_B$ . The G-AFM state remains stable at all simulated temperatures.

#### IV. DISCUSSION

In the ideal cubic  $\text{BaFeO}_3$  structure, all Fe cations are octahedrally coordinated by O anions and, thus, symmetrically equivalent. In the ideal monoclinic  $\text{BaFeO}_{2.67}$  structure, in contrast, four of the 12 Fe coordination polyhedra change from octahedra to tetrahedra due to the formation of the ordered vacancies on the O sites. As demonstrated in Sec. III B, the O atoms near the ordered vacancies mainly contribute to the dynamic instability. This may be intuited by considering that such O atoms have more space and, thus, can move more freely than the other atoms. The instability could also be related to a Jahn-Teller effect on the Fe cations at the tetrahedral sites, to which the +4 oxidation state was assigned previously by an analysis of bond valence sums [7]. For tetrahedral complexes, however, only a small impact of Jahn-Teller stabilization should be expected.

The ordered vacancies also induce additional anharmonicity in the investigated perovskites. Of course, both the vacancy-free cubic and the vacancy-ordered monoclinic structures are inherently anharmonic along the imaginary modes. As clarified by the double-well potentials [Figs. 3(e) and 5(b)], higher-order polynomials with even symmetry are required to stabilize the potential energies. Consistently, the trajectories at temperatures above the transition temperature (about 130 K) show an even-symmetric distribution along the symmetry-breaking direction ( $x$  in Fig. 4 and  $y$  in Fig. 6). For the vacancy-ordered monoclinic structure, moreover, an additional anharmonicity in the direction perpendicular to the symmetry-breaking direction is observed ( $z$  direction in Fig. 6). The trajectory distribution along this perpendicular direction is asymmetric, i.e., the O anion prefers on average to be located at positive  $z$  displacements. Thus, the creation of ordered vacancies induces an asymmetric local effective interatomic potential for some O atoms, specifically along the direction perpendicular to the symmetry-breaking direction.

With the DFT +  $U$  method, both the cubic and the monoclinic structures are predicted to be stabilized at about 130 K. As found in Fig. 3(e), HSE06 shows deeper potential wells than DFT +  $U$ , which indicates that the stabilization temperature predicted using HSE06 (in combination with AIMD) should be higher than 130 K for both the cubic and the monoclinic structures.

In contrast, quantum fluctuations, which are not included in AIMD, may decrease the stabilization temperature. In the case of  $\text{SrTiO}_3$ , for which displacement along an antiferrodistortive mode was shown to produce an energy decrease of about 10 meV/f.u. [29] (depending on the exchange-correlation functional), the transition temperature decreases from 130 to 110 K due to quantum fluctuations [45].

#### V. CONCLUSIONS

The structures of perovskites with ordered vacancies are much more complex than their vacancy-free cubic counterparts. This challenges an accurate determination of the exact arrangement of atoms. A particularly intricate aspect is the interplay of the ordered vacancies with the dynamic (in)stability of perovskites. In order to gain information on this interplay,

we have investigated the dynamic stability of the vacancy-free cubic  $\text{BaFeO}_3$  ( $Pm\bar{3}m$ ) and the vacancy-ordered monoclinic  $\text{BaFeO}_{2.67}$  ( $P2_1/m$ ) structures with AIMD in this paper.

Our results reveal that the ideal monoclinic structure for vacancy-ordered  $\text{BaFeO}_{2.67}$  is—in contrast to previous expectations [7]—dynamically unstable at 0 K. As temperature increases, the ideal monoclinic structure is dynamically stabilized at about 130 K. Interestingly, the ordered vacancies do not significantly alter the critical temperature at which Ba-Fe-O perovskites are dynamically stabilized. The calculated critical temperature is consistent with the dynamic stability requirement in the temperature range at which the high-symmetry phases are experimentally observed (about 300–700 K) [7]. From a broader perspective, similar results, i.e., dynamic instability at 0 K and stabilization at a relatively low temperature, may also be expected for the vacancy-ordered structures proposed for other perovskite-type phases composed of Ba, Fe, and O, or even other elements.

Additionally, we have found that strong anharmonicity is induced by the ordered vacancies for the monoclinic structure, along the direction perpendicular to the symmetry-breaking one. This can result in characteristic properties of the material, e.g., a small diffusion barrier of O atoms, which may contribute to fast ionic diffusion. Whereas the origin of fast ionic diffusion remains an interesting open question [46], our results provide hints for a possible atomistic mechanism.

#### ACKNOWLEDGMENTS

This project has received funding from the European Research Council (ERC) under the European Union's Horizon 2020 Research and Innovation Program (Grant Agreement No. 865855). The authors acknowledge support by the state of Baden-Württemberg through bwHPC and the German Research Foundation (DFG) through Grant No. INST 40/575-1 FUGG (JUSTUS 2 cluster). We also acknowledge support from the Stuttgart Center for Simulation Science (SimTech).

#### APPENDIX A: $U_{\text{eff}}$ PARAMETER SPACE FOR CUBIC $\text{BaFeO}_3$

Results obtained with DFT +  $U$  are sensitive to the input parameter  $U_{\text{eff}}$  as shown by Table I. We have explored the DFT +  $U$  parameter space by testing a range of  $U_{\text{eff}}$  values from 0 to 8 eV for FM cubic  $\text{BaFeO}_3$ . Figure 7(a) shows the  $U_{\text{eff}}$  dependence of the phonon dispersion. With a relatively small  $U_{\text{eff}}$  value ( $\leq 2$  eV), imaginary modes (indicating dynamic instability at 0 K) are found at all commensurate  $\mathbf{q}$  points included here, i.e.,  $\Gamma$ , M, R, and X. Less imaginary modes are present at larger  $U_{\text{eff}}$ . Specifically, imaginary modes at the M point disappear when  $U_{\text{eff}} \approx 6$  eV whereas at the R point they disappear when  $U_{\text{eff}} \approx 5$  eV. No imaginary mode is found for phonon calculations with a  $U_{\text{eff}}$  value larger than 7 eV. The result for  $U_{\text{eff}} = 5$  eV is found to be different from previous studies [15, 17] (cf. Table I), which may be due to the usage of different functionals or codes.

The dependence of the lattice constant on  $U_{\text{eff}}$  is shown in Fig. 7(b). With  $U_{\text{eff}} = 0$  eV (GGA functional), the calculated value is higher than the experimental value [27] (about 0.5%). The overestimation of the lattice constant predicted by the

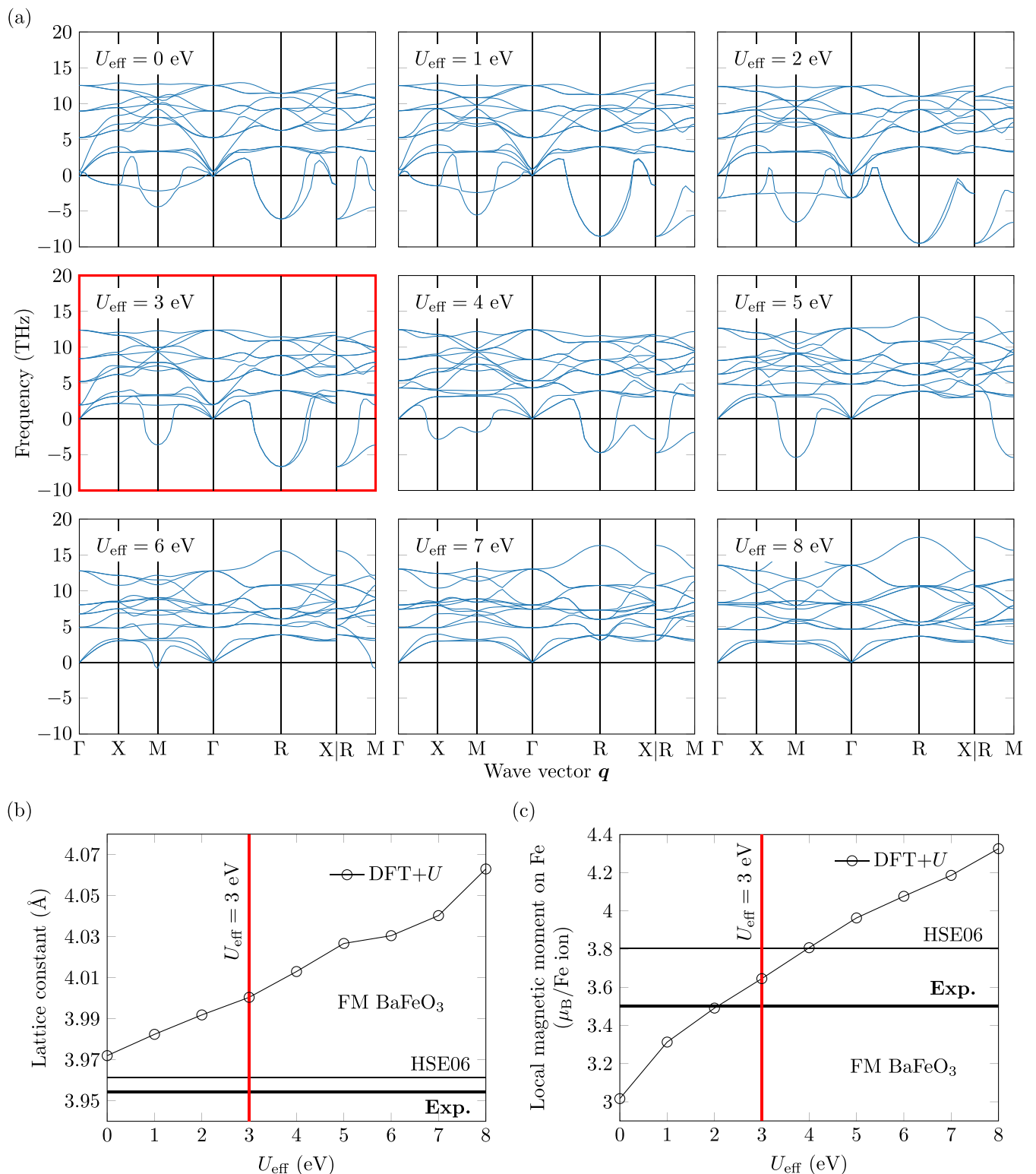


FIG. 7.  $U_{\text{eff}}$  dependence of (a) the phonon dispersion, (b) the lattice constant, and (c) the local magnetic moment on Fe for the FM cubic  $\text{BaFeO}_3$ . Results with  $U_{\text{eff}} = 3$  eV are highlighted by red lines. The phonon dispersion calculated by  $U_{\text{eff}} = 3$  eV is also shown in Fig. 3(b). Commensurate  $q$  points are indicated by tick labels. Imaginary modes are shown by negative frequencies. Experimental data are from Ref. [27].

TABLE II.  $U_{\text{eff}}$  values determined in previous studies for different oxidation states of Fe ions bound within O polyhedra.

Year	Methods	Fe oxidation states	$U_{\text{eff}}$ (eV)	Average $U_{\text{eff}}$ (eV)	Standard deviation (eV)
2006 [47]	Fitted to experiments	+2 $\rightarrow$ +3	3.90	4.00	0.14
		+2 $\rightarrow$ +2/+3	4.10		
2014 [48]	Fitted to experiments	+2	4.04	4.07	0.04
		+3	4.09		
2015 [49]	Linear response (QUANTUM-ESPRESSO <sup>a</sup> )	+2	4.10	3.76	0.32
		+2/+3	3.72		
		+3	3.47		
	Linear response (GBRV <sup>b</sup> )	+2	5.80	5.69	0.44
		+2/+3	6.07		
2019 [50]	Linear response (GBRV)	+2	6.28	6.21	0.36
		+3	5.82		
		+4	6.52		

<sup>a</sup>With the original QUANTUM-ESPRESSO [51,52] library.

<sup>b</sup>With the GBRV [53] ultrasoft pseudopotential set.

GGA functional has been also shown for the SrTiO<sub>3</sub> and the BaTiO<sub>3</sub> cubic perovskites [29]. The DFT +  $U$  method increases the amplitude of the overestimation. With  $U_{\text{eff}} = 3$  eV, the lattice constant is about 1% larger than the experimental value. The change in the local magnetic moment on the Fe atoms is shown in Fig. 7(c). The GGA functional underestimates the local magnetic moment by about 15%, which is corrected by the DFT +  $U$  method. With  $U_{\text{eff}} = 3$  eV, the calculated local magnetic moment is between the values given by experiments [27] and HSE06.

#### APPENDIX B: $U_{\text{eff}}$ TRANSFERABILITY TO MONOCLINIC BaFeO<sub>2.67</sub>

In vacancy-free cubic BaFeO<sub>3</sub>, Fe atoms are octahedrally coordinated and possess the +4 oxidation state. In the vacancy-ordered monoclinic BaFeO<sub>2.67</sub>, in contrast, Fe cations exist in the oxidation state of +3 rather than +4 [7].

Moreover, there are additional tetrahedrally and pyramidally coordinated Fe cations. The  $U_{\text{eff}}$  value suitable for these Fe cations could be different from 3 eV utilized for the cubic structure. It is challenging to calibrate the  $U_{\text{eff}}$  value directly for the monoclinic structure using the HSE06 hybrid functional due to the high computational cost. We have, therefore, pursued an alternate strategy to shed light on this aspect. Specifically, we have analyzed previous studies with respect to differences in the optimized  $U_{\text{eff}}$  values for Fe in different oxidation states in O polyhedra, with the key findings summarized in Table II. Whereas the absolute values of  $U_{\text{eff}}$  depend on the fitting parameters, the basis sets, the codes, etc., and are, thus, not immediately comparable, the small standard deviation of  $U_{\text{eff}}$  in each of the studies ( $< 0.50$  eV) indicates that  $U_{\text{eff}}$  is rather insensitive to the oxidation state of Fe. It is, thus, expected that the suitable  $U_{\text{eff}}$  values for the cubic and the monoclinic structures are similar. We have, therefore, focused on the  $U_{\text{eff}}$  values near 3 eV, i.e., 2–4 eV, and have

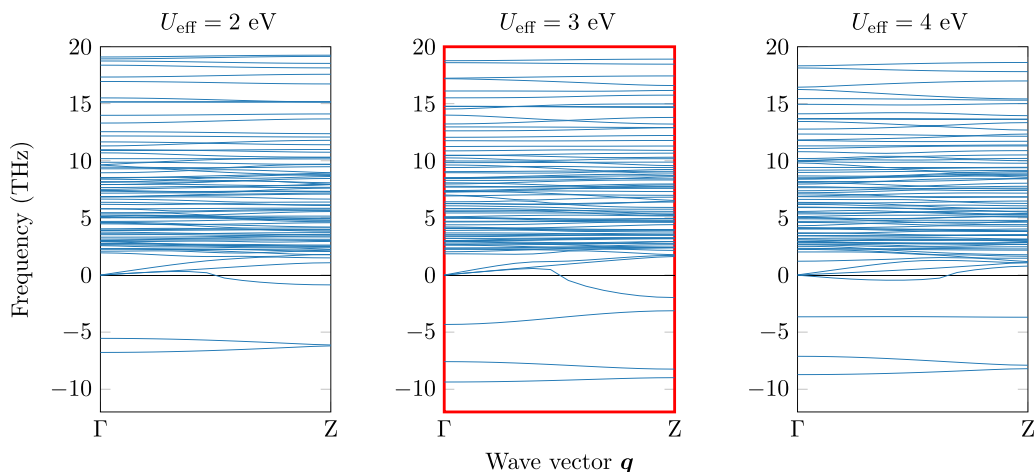


FIG. 8.  $U_{\text{eff}}$  dependence of the phonon dispersion for the G-AFM monoclinic BaFeO<sub>2.67</sub>. Results with  $U_{\text{eff}} = 3$  eV are highlighted by red lines and also shown in Fig. 5(a). The two points, i.e.,  $\Gamma = (0, 0, 0)$  and  $Z = (0, 0, 1/2)$ , are the commensurate  $q$  points for the utilized supercell. Imaginary modes are shown by negative frequencies.

calculated the phonon dispersions of the monoclinic structure also for these  $U_{\text{eff}}$  values as shown in Fig. 8. The four modes indicated in Fig. 5(a), i.e.,  $e_1^{\Gamma}$ ,  $e_2^{\Gamma}$ ,  $e_1^Z$ , and  $e_2^Z$ , are found to

be imaginary regardless of the  $U_{\text{eff}}$  values. The conclusions derived in Sec. III B should, therefore, not be affected by minor changes in  $U_{\text{eff}}$ .

- 
- [1] D. Shao, W. Zhu, G. Xin, J. Lian, and S. Sawyer, *Appl. Phys. Lett.* **115**, 121106 (2019).
- [2] M.-G. Ju, M. Chen, Y. Zhou, H. F. Garces, J. Dai, L. Ma, N. P. Padture, and X. C. Zeng, *ACS Energy Lett.* **3**, 297 (2018).
- [3] S. Sengodan, S. Choi, A. Jun, T. H. Shin, Y.-W. Ju, H. Y. Jeong, J. Shin, J. T. S. Irvine, and G. Kim, *Nature Mater.* **14**, 205 (2015).
- [4] A. Iqbal Waidha, H. Khatoun Siddiqui, Y. Ikeda, M. Lepple, S. Vasala, M. Donzelli, A. D. Fortes, P. Slater, B. Grabowski, U. I. Kramm, and O. Clemens, *Chem.-Eur. J.* **27**, 9763 (2021).
- [5] M. I. Gómez, G. Lucotti, J. A. de Morán, P. J. Aymonino, S. Pagola, P. Stephens, and R. E. Carbonio, *J. Solid State Chem.* **160**, 17 (2001).
- [6] O. Clemens, M. Gröting, R. Witte, J. M. Perez-Mato, C. Loho, F. J. Berry, R. Kruk, K. S. Knight, A. J. Wright, H. Hahn, and P. R. Slater, *Inorg. Chem.* **53**, 5911 (2014).
- [7] S. Wollstadt, Y. Ikeda, A. Sarkar, S. Vasala, C. Fasel, L. Alff, R. Kruk, B. Grabowski, and O. Clemens, *Inorg. Chem.* **60**, 10923 (2021).
- [8] V. M. Goldschmidt, *Naturwissenschaften* **14**, 477 (1926).
- [9] C. J. Bartel, C. Sutton, B. R. Goldsmith, R. Ouyang, C. B. Musgrave, L. M. Ghiringhelli, and M. Scheffler, *Sci. Adv.* **5**, eaav0693 (2019).
- [10] T. Sato, S. Takagi, S. Deledda, B. C. Hauback, and S. Orimo, *Sci. Rep.* **6**, 23592 (2016).
- [11] G. Kieslich, S. Sun, and A. K. Cheetham, *Chem. Sci.* **6**, 3430 (2015).
- [12] A. Togo and I. Tanaka, *Scr. Mater.* **108**, 1 (2015).
- [13] S. L. Dudarev, G. A. Botton, S. Y. Savrasov, C. J. Humphreys, and A. P. Sutton, *Phys. Rev. B* **57**, 1505 (1998).
- [14] E. O. Wollan and W. C. Koehler, *Phys. Rev.* **100**, 545 (1955).
- [15] I. Cherair, N. Iles, L. Rabahi, and A. Kellou, *Comput. Mater. Sci.* **126**, 491 (2017).
- [16] I. Cherair, E. Bousquet, M. M. Schmitt, N. Iles, and A. Kellou, *J. Phys.: Condens. Matter* **30**, 255701 (2018).
- [17] Y. Zhang, M. M. Schmitt, A. Mercy, J. Wang, and P. Ghosez, *Phys. Rev. B* **98**, 081108(R) (2018).
- [18] M. F. Hoedl, Electronic structure and defect chemistry in iron perovskites, Ph.D. thesis, University of Stuttgart, 2021.
- [19] J. P. Perdew, K. Burke, and M. Ernzerhof, *Phys. Rev. Lett.* **77**, 3865 (1996).
- [20] J. P. Perdew, A. Ruzsinszky, G. I. Csonka, O. A. Vydrov, G. E. Scuseria, L. A. Constantin, X. Zhou, and K. Burke, *Phys. Rev. Lett.* **100**, 136406 (2008).
- [21] J. P. Perdew, A. Ruzsinszky, G. I. Csonka, O. A. Vydrov, G. E. Scuseria, L. A. Constantin, X. Zhou, and K. Burke, *Phys. Rev. Lett.* **102**, 039902(E) (2009).
- [22] A. V. Krukau, O. A. Vydrov, A. F. Izmaylov, and G. E. Scuseria, *J. Chem. Phys.* **125**, 224106 (2006).
- [23] O. Hellman, I. A. Abrikosov, and S. I. Simak, *Phys. Rev. B* **84**, 180301(R) (2011).
- [24] T. Tadano and S. Tsuneyuki, *Phys. Rev. B* **92**, 054301 (2015).
- [25] J. Klarbring and S. I. Simak, *Phys. Rev. B* **97**, 024108 (2018).
- [26] T. Sun, D.-B. Zhang, and R. M. Wentzcovitch, *Phys. Rev. B* **89**, 094109 (2014).
- [27] N. Hayashi, T. Yamamoto, H. Kageyama, M. Nishi, Y. Watanabe, T. Kawakami, Y. Matsushita, A. Fujimori, and M. Takano, *Angew. Chem.* **123**, 12755 (2011).
- [28] S. Piskunov, E. Heifets, R. I. Eglitis, and G. Borstel, *Comput. Mater. Sci.* **29**, 165 (2004).
- [29] R. Wahl, D. Vogtenhuber, and G. Kresse, *Phys. Rev. B* **78**, 104116 (2008).
- [30] O. Clemens, *J. Solid State Chem.* **225**, 261 (2015).
- [31] K. Momma and F. Izumi, *J. Appl. Crystallogr.* **44**, 1272 (2011).
- [32] D. Korbmacher, A. Glensk, A. I. Duff, M. W. Finnis, B. Grabowski, and J. Neugebauer, *Phys. Rev. B* **100**, 104110 (2019).
- [33] Y. Ikeda, K. Gubaev, J. Neugebauer, B. Grabowski, and F. Körmann, *npj Comput. Mater.* **7**, 34 (2021).
- [34] K. Gubaev, Y. Ikeda, F. Tasnádi, J. Neugebauer, A. V. Shapeev, B. Grabowski, and F. Körmann, *Phys. Rev. Materials* **5**, 073801 (2021).
- [35] Z. Li, R. Laskowski, T. Iitaka, and T. Tohyama, *Phys. Rev. B* **85**, 134419 (2012).
- [36] B. Ribeiro, M. Godinho, C. Cardoso, R. P. Borges, and T. P. Gasche, *J. Appl. Phys.* **113**, 083906 (2013).
- [37] I. V. Maznichenko, S. Ostanin, L. V. Bekenov, V. N. Antonov, I. Mertig, and A. Ernst, *Phys. Rev. B* **93**, 024411 (2016).
- [38] G. Rahman, J. M. Morbec, R. Ferradás, V. M. García-Suárez, and N. J. English, *J. Magn. Magn. Mater.* **401**, 1097 (2016).
- [39] P. E. Blöchl, *Phys. Rev. B* **50**, 17953 (1994).
- [40] G. Kresse, *J. Non-Cryst. Solids* **192-193**, 222 (1995).
- [41] G. Kresse and J. Furthmüller, *Phys. Rev. B* **54**, 11169 (1996).
- [42] G. Kresse and D. Joubert, *Phys. Rev. B* **59**, 1758 (1999).
- [43] M. Methfessel and A. T. Paxton, *Phys. Rev. B* **40**, 3616 (1989).
- [44] P. E. Blöchl, O. Jepsen, and O. K. Andersen, *Phys. Rev. B* **49**, 16223 (1994).
- [45] W. Zhong and D. Vanderbilt, *Phys. Rev. B* **53**, 5047 (1996).
- [46] S. Wollstadt, R. A. De Souza, and O. Clemens, *J. Phys. Chem. C* **125**, 2287 (2021).
- [47] L. Wang, T. Maxisch, and G. Ceder, *Phys. Rev. B* **73**, 195107 (2006).
- [48] M. Aykol and C. Wolverton, *Phys. Rev. B* **90**, 115105 (2014).
- [49] Z. Xu, Y. V. Joshi, S. Raman, and J. R. Kitchin, *J. Chem. Phys.* **142**, 144701 (2015).
- [50] J. W. Bennett, B. G. Hudson, I. K. Metz, D. Liang, S. Spurgeon, Q. Cui, and S. E. Mason, *Comput. Mater. Sci.* **170**, 109137 (2019).
- [51] P. Giannozzi, S. Baroni, N. Bonini, M. Calandra, R. Car, C. Cavazzoni, D. Ceresoli, G. L. Chiarotti, M. Cococcioni, I. Dabo, A. D. Corso, S. de Gironcoli, S. Fabris, G. Fratesi, R. Gebauer, U. Gerstmann, C. Gougoussis, A. Kokalj, M. Lazzeri,

- L. Martin-Samos *et al.*, *J. Phys.: Condens. Matter* **21**, 395502 (2009).
- [52] P. Giannozzi, O. Andreussi, T. Brumme, O. Bunau, M. B. Nardelli, M. Calandra, R. Car, C. Cavazzoni, D. Ceresoli, M. Cococcioni, N. Colonna, I. Carnimeo, A. D. Corso, S. de Gironcoli, P. Delugas, R. A. DiStasio Jr., A. Ferretti, A. Floris, G. Fratesi, G. Fugallo *et al.*, *J. Phys.: Condens. Matter* **29**, 465901 (2017).
- [53] K. F. Garrity, J. W. Bennett, K. M. Rabe, and D. Vanderbilt, *Comput. Mater. Sci.* **81**, 446 (2014).